Initial Results of the Geostationary Synthetic Thinned Array Radiometer (GeoSTAR) Demonstrator Instrument

Alan B. Tanner, William J. Wilson, *Fellow, IEEE*, Bjorn H. Lambrigsten, Steve J. Dinardo, *Associate Member, IEEE*, Shannon T. Brown, *Member, IEEE*, Pekka P. Kangaslahti, Todd C. Gaier, Christopher S. Ruf, *Fellow, IEEE*, Steven M. Gross, Boon H. Lim, Stephen B. Musko, Steven A. Rogacki, and Jeff R. Piepmeier

***Abstract*—The design, error budget, and preliminary test results of a 50–56-GHz synthetic aperture radiometer demonstration system are presented. The instrument consists of a fixed 24-element array of correlation interferometers and is capable of producing calibrated images with 1° spatial resolution within a 17° wide field of view. This system has been built to demonstrate a performance and a design which can be scaled to a much larger geostationary Earth imager. As a baseline, such a system would consist of about 300 elements and would be capable of providing contiguous full hemispheric images of the Earth with 1 K of radiometric precision and 50-km spatial resolution. An error budget is developed around this goal and then tested with the demonstrator system. Errors are categorized as either scaling (i.e., complex gain) or additive (noise and bias) errors. Sensitivity to gain and/or phase error is generally proportional to the magnitude of the expected visibility, which is high only in the shortest baselines of the array, based on model simulations of the Earth as viewed from geostationary Earth orbit. Requirements range from approximately 0.5% and 0.3° of amplitude and phase uncertainty, respectively, for the closest spacings at the center of the array, to about 4% and 2.5° for the majority of the array. The latter requirements are demonstrated with our instrument using relatively simple references and antenna models, and by relying on the intrinsic stability and efficiency of the system. The 0.5% requirement (for the short baselines) is met by measuring the detailed spatial response (e.g., on the antenna range) and by using an internal noise diode reference to stabilize the response. This result suggests a hybrid image synthesis algorithm in which long baselines are processed by a fast Fourier transform and the short baselines are processed by a more precise (G-matrix) algorithm which can handle small anomalies among antenna and receiver responses. Visibility biases and other additive errors must be below about 1.5 mK on average, regardless of baseline. The bias requirement is largely met with a phase-shifting scheme applied to the local oscillator distribution of our demonstration system. Low mutual coupling among the horn antennas of our design is also critical to minimize the biases caused by crosstalk of receiver noise. Performance is validated by a three-way comparison between interference fringes measured on the antenna range, solar transit observations, and the system model.**

Manuscript received May 30, 2006; revised November 3, 2006.

A. B. Tanner, W. J. Wilson, B. H. Lambrigsten, S. J. Dinardo, S. T. Brown, P. P. Kangaslahti, and T. C. Gaier are with the Jet Propulsion Laboratory, California Institute of Technology, Pasadena, CA 91125 USA (e-mail: Alan.b.tanner@jpl.nasa.gov).

C. S. Ruf, S. M. Gross, B. H. Lim, S. B. Musko, and S. A. Rogacki are with the University of Michigan, Ann Arbor, MI 48109 USA.

J. R. Piepmeier is with the Goddard Space Flight Center, Greenbelt, MD 20771 USA.

Digital Object Identifier 10.1109/TGRS.2007.894060

***Index Terms*—Interferometry, microwave imaging, microwave radiometry, remote sensing.**

I. Introduction

THE GEOSTATIONARY Synthetic Thinned Array Radiometer (GeoSTAR) is a concept to provide high spatial resolution soundings of the Earth's atmosphere from geosynchronous Earth orbit (GEO) in discrete microwave bands from 50 to 180 GHz [1]. Images of the Earth are synthesized by a Fourier transform of interferometric data collected with a Y-array of correlation interferometers. The concept eliminates the need for large mechanically scanned apertures, but it poses many new challenges—particularly in the area of calibration. A large spaceborne system will involve hundreds of antennas and many tens of thousands of correlators. Costs associated with design choices will be high. Therefore it is important to develop an error model and to demonstrate how the requirements will be met with real hardware. This paper presents the preliminary results of a small (24-element) 50–56-GHz system which has been built under the NASA's Instrument Incubator Program to provide such a demonstration.

Our design is based on aperture synthesis techniques originally developed for radio astronomy and applied more recently to Earth remote sensing. The first such application was the Electronically Scanned Thinned Array Radiometer (ESTAR) [2], which was a 1-D synthesis array operating at L-band to measure soil moisture. This small (five-element) aircraft system viewed a wide pushbroom swath and was subject to a high degree of mutual coupling and array embedding effects which were difficult to model. This problem lead to the so-called G-matrix calibration, where images are synthesized by an inversion of interferometric fringes measured on the antenna range [3]. With this approach, the accuracy of the images depends on the quality of the antenna range measurements and the degree to which such measurements accurately represent the operational configuration (i.e., as installed in an aircraft or spacecraft structure). More recently, the European Space Agency has advanced the microwave imaging radiometer by an aperture synthesis instrument for the soil moisture ocean salinity mission. Scheduled for launch in 2007, this 69-element system is a 2-D imager configured as a Y-array of closely spaced patch antenna elements with a wide field of view (FOV) appropriate for low Earth orbit. Like

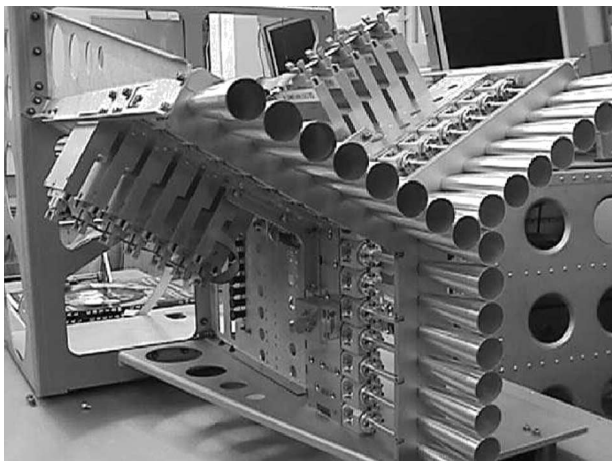

Fig. 1. GeoSTAR demonstrator instrument.

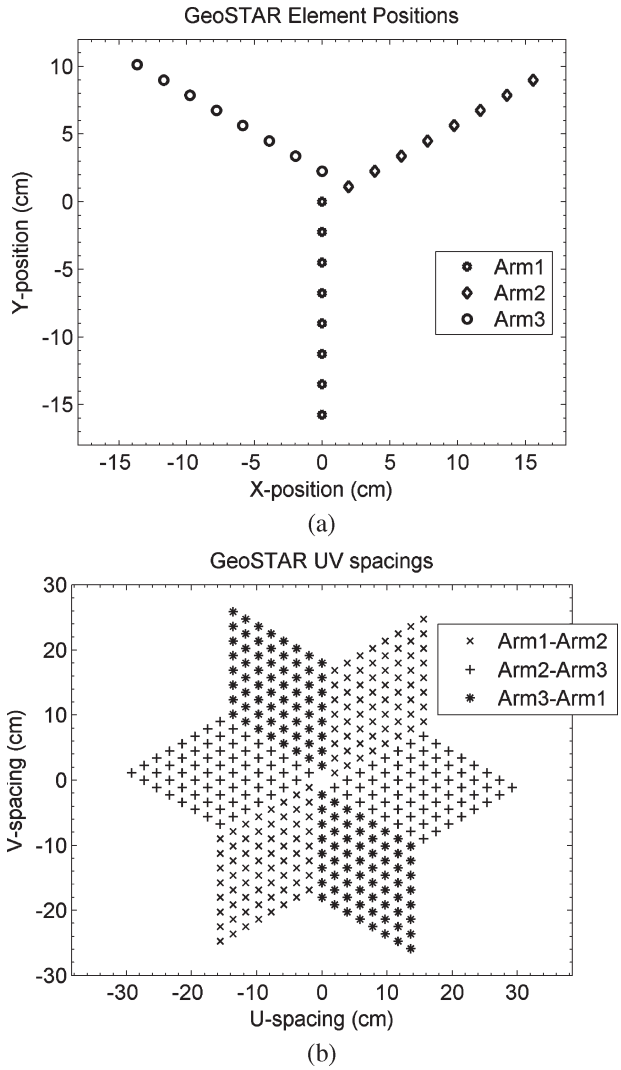

Fig. 2. Antenna array layout (a) and corresponding UV samples of the synthetic aperture. (b) Each u-v sample is a difference between x and y positions of two antennas (i.e., for antennas A and B $u_{\mathrm{AB}} = x_{\mathrm{A}} - x_{\mathrm{B}}, v_{\mathrm{AB}} = y_{\mathrm{A}} - y_{\mathrm{B}}$).

ESTAR, the broad antenna pattern of this system is subject to significant array embedding effects and mutual coupling which must be precisely measured and then accounted for in the inversion [4]–[6]. These measurements are quite costly and possibly impractical for GeoSTAR. A large system with 300 elements or more is envisioned for each of the three observation bands of the GeoSTAR. It will be difficult to measure the G-matrix with very high precision for such a large array. Moreover, the inversion of such a large data set—which would involve the inversion of a $60\,000 \times 60\,000$ matrix—poses a major challenge in itself.

Our approach in GeoSTAR is to seek a design which does not depend so heavily on the measurements of the antenna responses nor on the inversion of such large matrices. To the extent possible, we seek a design which can be characterized by a single well-matched antenna pattern which is predictable and uniform among all elements of the array. If this can be achieved, then the synthesis problem becomes much simpler and can possibly be performed by a much more efficient Fast Fourier Transform (FFT) [7]—rather than the numerically intensive G-matrix. One advantage with the GeoSTAR is that the observations of the Earth are made within a relatively narrow 17° wide FOV. This allows for a larger elemental antenna aperture, which offers more design options to reduce mutual coupling and other array embedding problems.

Following an overview of the instrument concept in Section II, we present an error budget in Section III. This establishes some priorities for the design which is presented in Section IV. Processing algorithms are discussed in Section V, along with some preliminary test results. The end-to-end performance is measured on the antenna range in Section VI, and sample images are presented in Section VII. Some fundamentals of the interferometer mathematics and of the synthesis process are summarized in the Appendix for reference.

II. Instrument Concept

GeoSTAR consists of a Y-array of receivers configured in the geometry in Figs. 1 and 2. The antennas share the same FOV, and the IF signals of all receivers are simultaneously cross-correlated against one another in a digital subsystem. Each correlated antenna pair forms an interferometer which measures a particular spatial harmonic of the brightness temperature across the FOV. When expressed as a function of antenna spacing—or "baselines" with dimensions u and v by astronomy convention—this complex cross correlation is called the visibility function and is denoted as $V(u, v)$. The visibility function is the Fourier transform of the brightness temperature image in the FOV, as weighted by the elemental antenna pattern. The mathematics of this technique are well established and summarized in Appendix I for reference. With a sufficient sampling of visibility over a range of spacings, one can reconstruct or synthesize a 2-D image by an inverse transform. The "Y" configuration provides the needed samples using a minimum number of antennas and with a fixed geometry—in a so-called thinned array. As shown in Fig. 2, the spacings between the various antenna pairs yield a uniform hexagonal grid of visibility samples in the u-v plane. There are $n = 8$ elements in each arm in Fig. 2, and this yields $n^2 = 64$ unique u and v spacings when the x and y positions of arm 1 are subtracted from arms 2,

for example. Another 64 conjugate-symmetric samples are derived by subtracting arm 2 from arm 1. In all, the system produces 384 complex visibility samples $(= 6n^2)$. Note that in this particular layout, all of the u-v samples are formed between the elements in different arms. We do not need (and, in fact, do not use) any correlations among the elements of a common arm. This scheme (we call the "staggered-Y") simplifies the electrical and mechanical designs, as detailed in Section IV.

The smallest spacing of the sample grid in Fig. 2 determines the unambiguous FOV (UaFOV), which for GEO observations has a special interpretation. For the hexagonal u-v sample grid with spacing d in Fig. 2, sources in the FOV are aliased periodically every $(2/\sqrt{3})(\lambda/d)$ radians in the image plane along three axes: one horizontal and two diagonals separated by 120°. This establishes a hexagonal region within which images are synthesized [7]. In our application, we fit this region to match the Earth disk diameter of 17.5° when viewed from the GEO. This sets both the element spacing and diameters at about 3.75 wavelengths, assuming a full-disk coverage is required. Our design actually sets the spacing at 2.25 cm, which provides a full-disk coverage at 50.3 GHz, and some aliasing at 56 GHz near the limb where the local incidence angles are otherwise too shallow for atmospheric sounding. But note that, strictly speaking there is no "unambiguous" FOV for GeoSTAR. The elemental antenna patterns do not end abruptly at the edge of the synthesized image. Therefore the brightness from the surrounding (aliased) regions must be known and corrected in the image processing. In space this does not pose a problem since the temperature of the cosmic background is well known. But this does play a role in our ground-based demonstrator instrument, which must be tested in an ambient environment.

The longest spacing determines the smallest spatial scale that can be resolved. For the array in Fig. 1 with $n = 8$ elements per arm and $d = 2.25$ cm, the synthesized half-power beamwidth is $1.0°$ $(= 0.53\lambda/\mathrm{nd}$ radians) at 50.3 GHz. A large spaceborne system at 36 000-km altitude, with 50-km resolution, will require $0.08°$ of resolution and 100 elements per arm using this half-power criteria [2], [8]. An alternative measure of the resolution can be derived from the number of independent pixels per unit area within the image: the Fourier Transform provides a one-to-one mapping, which ensures that there are as many linearly independent pixels as linearly independent visibility samples. Our system provides $6n^2$ linearly independent samples[1] within a hexagonal FOV of area $(2/\sqrt{3})(\lambda^2/d^2)$, and this implies a linear resolution of $(\lambda/\mathrm{nd})\sqrt{2/6\sqrt{3}}$ or $0.44(\lambda/\mathrm{nd})$ radians in the square root.

III. Error Budget

Our design is based on an overall calibration requirement of 1-K error in the synthesized brightness temperature image of the Earth using a large array of 300 elements. Our analysis arbitrarily divides the error budget equally between categories of "gain" and of "additive" errors. Gain and additive errors are presumed independent; therefore, an equal split of the 1-K overall error implies 0.7 K $(= 1\ \mathrm{K}/\sqrt{2})$ allocations for each of these categories. Gain errors include anything that results in an uncertain amplitude scaling or phase shift in the visibility measurements. These include uncertainties in elemental antenna patterns and array alignment, as well as uncertainties of the gain, efficiency, and phase response of the correlators. Additive errors include correlator biases (null offsets) and measurement noise (set by system noise, bandwidth, and integration time). Additive errors are measured in units of Kelvin, whereas the gain errors are expressed as a percentage and/or degrees of phase and must be scaled to Kelvin by the magnitude of the expected signal. Gain is a complex value; therefore gain and phase error specifications are often redundant. For example, 0.01 radian of the phase error usually has the same impact as 1% of the gain magnitude error since they both represent the same displacement of visibility in the complex plane.

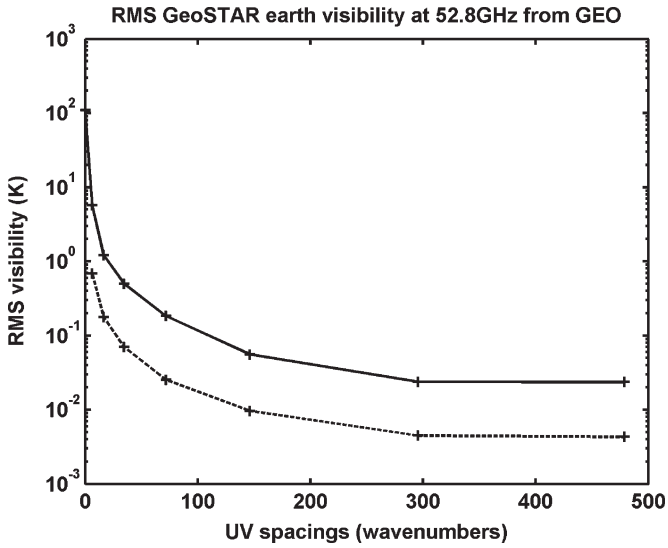

Fig. 3. RMS GeoSTAR visibility versus UV radius using AMSU 52.8 GHz brightness temperatures. The dashed line represents the variability within the Earth disk after having removed the mean Earth temperature and limb contrast.

In the simplest analysis of the gain errors, we can divide the 0.7-K budget allocation by an approximate 260-K mean Earth temperature to arrive at a requirement of 0.3% $(= 0.7\ \mathrm{K}/260\ \mathrm{K})$ to be applied uniformly to the entire array. Yet, this is a difficult requirement to meet, and we know that most of the signal in the GeoSTAR is contained in the shortest baselines of the visibility function. A better analysis takes this into account. Fig. 3 plots the rms magnitude of visibility versus u-v baseline, as computed from an AMSU 52.8-GHz brightness temperature map of the Earth with the current GeoSTAR antenna model. Here, we see that only the zero-baseline channel exceeds 100 K, and that, only the shortest baselines of less than 20 wavenumbers are in the 1–5-K range. Past about 100 wavenumbers, the visibilities are well below

[1]Here, we have counted the independent samples in Fig. 2. We note that although there is a twofold redundancy in Fig. 2 [since $V(u, v)$ is the conjugate of $V(-u, -v)$], that the in-phase and quadrature-phase components of each complex correlation are linearly independent. Thus, there are still $6n^2$ linearly independent measurements from which $6n^2$ (real valued) image pixels may be synthesized.

TABLE I
VISIBILITY GAIN ERROR BUDGET, BASED ON GeoSTAR VISIBILITIES COMPUTED WITH AMSU DATA IN FIG. 3

$\sqrt{u^2+v^2}$ range[1] (wavenumber)	count[2]	RMS[3] (K)	RSS[4] (K)	ΔG[5] (%)	ΔT[6] (K)
0 - 3	1	108.8	108.8	0.1	0.25
3 - 9	9	5.7	17.0	0.7	0.25
9 - 21	45	1.2	8.2	1.5	0.25
21 - 45	177	0.5	6.6	1.9	0.25
45 - 93	765	0.18	5.1	2.4	0.25
93 - 189	3126	0.056	3.1	4.0	0.25
189 - 381	12639	0.024	2.7	4.6	0.25
381 - 683	13239	0.024	2.7	4.6	0.25
net:	30,001				0.7

notes:
1. Range of radii from center of u-v plane specify annular rings on u-v plane.
2. "count" of independent complex visibility samples which fall in each range.
3. RMS visibility in this u-v range (from Fig. 3).
4. RSS visibility in this range (=RMS*SQRT(count)).
5. Gain error allocation for these visibilities which result in a net 0.7K delta-T in the image, as computed from 0.7K/(2*RSS*root(8)). The factor of 2 accounts for antenna pattern beam efficiency within the earth disk, and the root(8) represents the number of u-v range bins in this table.
6. Image delta-T allocated to this range bin (=0.7 K gain allocation / SQRT(8))

0.1 K.[2] This indicates that the GeoSTAR should be much less sensitive to the gain errors for larger baselines. This is good from a hardware standpoint since, for example, it permits greater mechanical error toward the ends of the array arms. Yet it is not appropriate to allocate too much error to the longer baselines since there is a great many more of these visibilities. A more judicious distribution of errors is needed which balances the practical hardware limitations with the sensitivities and numbers of correlators in the overall array.

Table I provides a gain budget that accounts for both the magnitudes and the numbers of visibility samples. Here, we have grouped the visibilities by their distance from the center of the u-v plane and distributed the errors by applying the rule that image errors are the root-sum-square (RSS) of visibility errors.[3] In order to distribute the error allocations in a reasonable manner, Table I subjectively divides the u-v plane into eight annular regions, centered on the origin, as specified with the u-v radii in the first column. These regions are progressively larger (roughly in powers of 2 with each region) and encompass ever greater numbers of visibility samples (in column 2) with distance from the origin. The rms visibilities in Fig. 3 are summarized in column 3, but it is the RSS visibility in column 4 and the 0.25-K delta-T $(= 0.7\ \text{K}/\sqrt{8})$ allocation in column 6 that determine the delta-G error allocation in column 5. The delta-G requirement is computed as $0.5 *$ delta-T divided by the RSS visibility. The factor of 0.5 is a nominal number which is needed to account for the antenna pattern scaling which occurs during the image synthesis. For GeoSTAR and as discussed in the next section and Appendix I, this amounts to a scaling by a factor of about 1.6 near the center of the FOV and about three near the Earth limb. We use a nominal factor of 2 here, but note that there is an inherent degradation of delta-T near the edges of the image plane where the antenna beam tapers off. Also note that Table I is based on the RSS of 30 000 complex visibilities, and that, (with the exception of the zero-baseline visibility of the first row, which is real valued) the "gain" errors are understood to be complex gain errors. These can be further broken down into constituent phase and magnitude errors.

Table I shows that a 4% gain error is acceptable for the great majority of visibility samples. This corresponds to about 2.3° of phase error in the complex plane (or about 0.2 mm of mechanical alignment for the 0.6-cm wavelength). Only a few baselines near the center of the array need a more precise calibration. This establishes top level gain requirements for the correlators and must be further divided into allocations for array distortions, receiver gain, and antenna pattern errors. The zero-baseline visibility is the only channel requiring a 0.1% calibration. This will actually be measured with a conventional Dicke radiometer (not shown in Figs. 1 or 2) using an identical antenna to those in the rest of the array. The error allocations in Table I change only slightly if the array size increases or decreases.

Additive errors include correlator biases (null offsets) and the basic measurement noise set by system noise, bandwidth, and integration time. The latter is relatively constant among all visibility samples; therefore, it is necessary on average to keep this noise below $0.5 * 0.7$ K/SQRT(N), where N is the number of visibility samples in the Fourier series. Here, we have again applied the rule that image errors are the RSS of visibility errors, and the factor of 0.5 again accounts for the scaling of the Earth image by the antenna pattern. With $N = 60\,000$ samples, the rms visibility errors must be less than about 1.5 mK. The visibility noise (delta-V) for bandwidth B, integration time τ, and system noise temperature $T_{\rm s}$ using a 1-bit correlator is

$$\Delta V = \frac{\pi}{2}\frac{T_{\rm s}}{\sqrt{2B\tau}}. \tag{1}$$

where $(\pi/2)$ accounts for the change in sensitivity which results from the mapping of a 1-bit correlation to a linear correlation with the Van Vleck formula [9]. The system noise is about 500 K in our instrument, and the double sideband bandwidth is 200 MHz. Therefore, 1.5 mK implies a minimum of $\tau = 740$ s. This is a minimum which does not yet allocate any of the additive budget to the visibility biases. We wish to avoid in increasing this integration time any further. Therefore

[2]GeoSTAR visibilities are dominated by the contrast at the Earth's limb in all observation bands. The dashed line in Fig. 3 represents the same data after subtracting the constant temperature from the Earth disk. This dashed line shows that the contribution from variability within the Earth is nearly an order of magnitude smaller than the contribution from the limb. This is interesting because it shows how requirements might change if GeoSTAR were provided an initialization from other sources (e.g., low-Earth-orbit observations or climate averages). However, our present goal is an absolute (not relative) calibration, so we do not yet consider this in our error budget.

[3]This is a basic property of the Fourier series (energy conservation), and worth noting because it is central to the discussion: To a first order, the rms brightness of the image is always equal to the RSS of the visibilities. One Kelvin applied to N visibility samples always adds $\sqrt{N}$ Kelvin to the rms brightness temperature. It does not matter whether the visibilities are coherent or random in phase, provided that the rms temperature is evaluated over the entire image plane. This relation is only modified if we weight the aperture (e.g., to change sidelobe levels) or scale the image to compensate for the antenna patterns or mismatches among receivers.

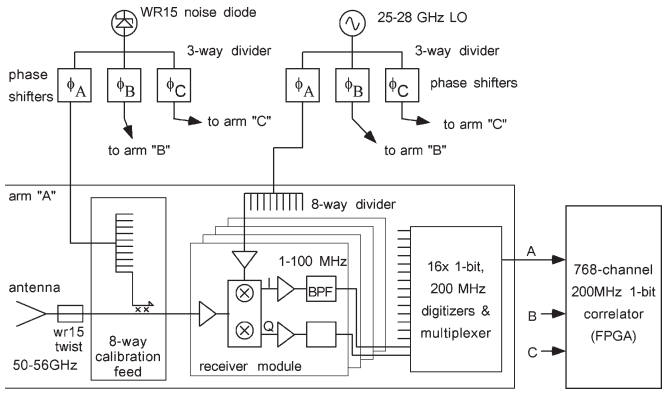

Fig. 4. System block diagram—one receiver of 24 shown.

we will pursue a design which keeps biases well below the measurement noise. Our results, as discussed below, show that extremely small biases of 0.5 mK are achievable for back-end errors [e.g., digitizer null offsets and common mode noise from the local oscillator (LO)]. The mutual coupling of front-end receiver noise between antennas ultimately dominates the biases otherwise. But this problem is found to be prevalent only in the short baselines of the array where the coupling is highest. This is permissible since these short baselines represent a small fraction of the complete array.

IV. Demonstrator Instrument

The GeoSTAR demonstrator instrument operates at four AMSU channels between 50 and 56 GHz. A simplified block diagram is given in Fig. 4. From left to right in Fig. 4 (or front to back in Fig. 1), the signal starts at the horn apertures with horizontal polarization. The horns are a variant of a Potter horn which adds a parabolic profile section to broaden the useful RF band to 50–56 GHz. The design permits very close spacing in the array while maximizing the aperture area. This is important for the GEO observation as it maximizes the fraction of the antenna energy which is received from the Earth disk. This fraction (we call "Earth disk beam efficiency") is about 42% with this design. We also tested a straight taper conical horn with a uniform E-plane illumination which increases this fraction to 48%. However, the mutual coupling of that horn is high, and when tested on the antenna range, we found that this design was subject to significant array embedding effects which perturbed the radiation patterns at the 5% to 10% level. The aperture taper provided by the parabolic Potter design reduces these effects, which simplifies the antenna modeling problem. The low coupling is also crucial for controlling the correlation biases caused by the leakage of receiver noise from one antenna to another. To further suppress the biases from coupling, ferrite isolators (not shown in the diagram) are added to the six closest elements at the center of the array where the coupling is greatest (about -60 dB between adjacent elements). Beyond these elements, the majority of the array operates without isolators. This strategy lowers the overall noise figure of the system.

Each horn incorporates a circular to rectangular transition, followed by a waveguide twist of either 0, $+60$, or -60° to match the orientation to the three arms in Fig. 1. These twists provide a simple and precise polarization alignment. We considered circular polarizers, but found that they were not easily balanced through the 10% bandwidth.

The signal in Fig. 4 next passes through an eight-way calibration feed manifold which periodically injects a noise signal into all receivers from a common noise diode source. This signal provides a reference to stabilize the system against gain, phase, and receiver noise drifts. The injected signal reaches the receiver inputs with about 5-K equivalent noise temperature. The noise diode signal is distributed to the three arms via phase shifters. These shifters were intended as a means to resolve the quadrature balance of each correlator, but later proved redundant with other circuits described below.

Next, the antenna signal passes into the monolithic microwave integrated circuit receiver module where it is amplified using InP FET low noise amplifiers (LNAs) and then double-sideband downconverted by subharmonic quadrature mixers to two IF baseband signals. Receiver noise is about 400 K. Each receiver also contains a programmable bias circuit which can adjust the gate and drain voltages of each amplifier stage to affect gain and noise figure. This circuit was originally envisioned as another calibration tool (e.g., to switch off a receiver and, thereby, measure the correlator biases), but it proved more useful to balance and tune the receivers during production and tests. The gain of the RF section is about 50 dB. We operate with such high gain to minimize the impact of common mode noise from the LO, which will otherwise bias the correlations.

The LO in Fig. 4 operates from 25 to 28 GHz to tune from 50 to 56 GHz at RF. The LO is distributed via three 2-bit phase shifters and amplifiers which incorporate power levelers. These periodically shift the phase to each arm by 45°, 90°, or 135°, which results in shifts of 90°, 180°, and 270°, respectively at RF. Constant LO power is ensured by an active circuit consisting of a coupled detector with a feedback to control the LO amplifier gain. As discussed in Section V, this circuit proved superior to the above noise diode phase shifters and to the RF amplifier controls when estimating the quadrature balance and correlator biases. We should also add that the staggered Y-array in Fig. 2 is a key to this scheme since we only need to shift the phase between arms—not between elements within an arm.

The in-phase (I) and quadrature (Q) IF signals from each mixer are next amplified and low-pass filtered at 100 MHz. These are small and inexpensive lumped element filters. The phase match among these filters is excellent across the band, resulting in very high ($> 99\%$) efficiency in the correlators. The IF signals are then digitized at a clock rate of 200 MHz. For reasons of product availability, the analog-to-digital converters are presently 8-bit devices, but these could be replaced with 1-bit converters (i.e., comparators). The correlators only use 1-bit (the sign bit). One-bit correlators require the least power with a relatively minor penalty in sensitivity, which is a fair tradeoff given the great number of correlators required by GeoSTAR. The correlator in Fig. 4 is implemented in a field programmable gate array. This system calculates all possible correlations to be formed between the 24 elements, but we actually only use the correlations which are formed between the different array arms. We do not use the correlations formed among elements within each arm because of several problems: 1) There

is an RF leakage that occurs between receivers within the eight-way calibration feed in Fig. 4 that cannot be easily eliminated; 2) the LO phase modulation does not apply; and 3) there is almost no benefit to the image synthesis problem. Note that these along-arm correlations are redundant to less than 1% of the u-v samples in a 300-element array (since there are only 600 along-arm baselines out of 60 000 total); therefore, even with a "perfect" performance, the reduction of RSS errors would be less than 0.5% (i.e., no less than a factor of $\sqrt{59\,400/60\,000}$ noise reduction).

V. Data Processing and Early Test Results

The 1-bit correlations are first mapped to linear correlations using the Van Vleck formula [9]. This removes the nonlinearity of a 1-bit correlator when the input signals are known to be Gaussian. This step is applied to all four correlators associated with each antenna pair. Each antenna is associated with an "I" and a "Q" IF signal; therefore, each antenna pair is associated with four correlators: "II," "QQ," "QI," and "IQ." This represents a twofold redundancy in our data which we use to reduce the measurement noise. If there were no biases and if the subharmonic mixers in Fig. 4 were perfectly balanced in quadrature, then these four correlations could be immediately combined into a single complex correlation. Yet, the quadrature balance is known to be poor—on the order of 10° of phase—and the raw correlations are known to contain large biases due to digitizer null offsets and leakage of the correlated noise from the LO. To fix this, the LO phases are shifted in a sequence that rotates all correlations to all four phase quadrants. The exact phase shifts are determined from network analyzer measurements made prior to system integration. These are applied in a linear regression to resolve the amplitude, offset, and phase of each correlator. This yields four redundant complex correlations which are averaged to form the final estimate. This process ensures very precise quadrature balance and virtually eliminates the biases caused by anything other than direct leakage of the RF signals among the antennas. Currently, we have observed total biases ranging from about 3 to 40 mK in the shortest baselines, due almost entirely to the leakage between antennas. This has contributed a net 0.5 K to the raw synthesized image errors. These errors are also very stable and readily corrected to the 0.1-K level. We expect that these biases will continue to diminish to acceptable levels for the larger array. Therefore we do not anticipate a problem. We have also conducted separate tests with the isolated receivers which show back-end biases at the 0.5-mK level after many thousands of seconds of integration time, which meets our goals for the larger array.

The above correlations are next scaled to visibility using an estimate of the system noise temperature and then aligned in phase to the aperture plane. We have thus far used LN2 and ambient targets to estimate the receiver noise temperature and point sources on an antenna range to align the phase. These references are transferred to operations by at least two methods: The first uses the internal noise diode to deflect the correlation and system noise by a reliable amplitude and phase. This provides a convenient and steady reference, but there are noise penalties due to the time required to measure the noise diode. The second method relies on the intrinsic stability of the receivers. The receiver noise temperatures of GeoSTAR are quite stable at the ∼2-K level, which represents about 0.4% of the ∼500-K system noise. The observed phase stability is better than ∼1°. These stabilities readily satisfy the phase and amplitude needs of most correlators in Table I. To meet the stricter phase requirements for correlations near the center of the u-v plane, we will likely need the noise injection. This is an ongoing study, but we now envision a hybrid scheme which uses long running averages of low duty cycle noise diode injection—applied only to those correlators near the center of the u-v plane. The larger baselines should not need this reference circuit, which comes at considerable costs.

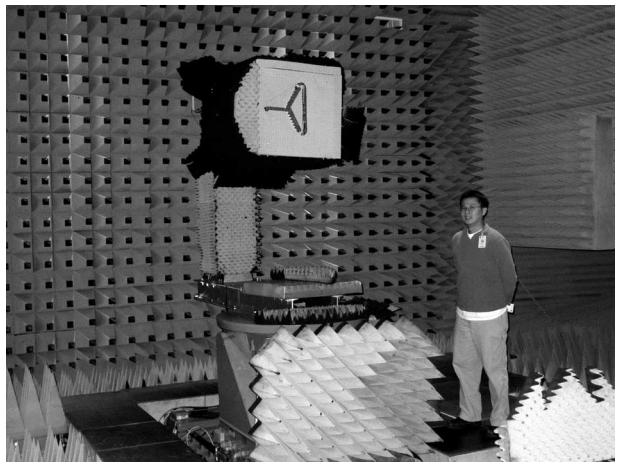

Fig. 5. GeoSTAR as tested on the CR. The "Y" array is rotated here by 90° in polarization. The system is otherwise wrapped in absorber material to reduce reflections on the range.

The visibilities are next transformed into an image. Ideally, this step is a Fourier transform, followed by a scaling within the Earth disk by the elemental antenna pattern. Details are referred to Appendixes I and II.

VI. Antenna Range and Solar Transit Tests

In October of 2005, the completed GeoSTAR demonstrator was tested on a compact range (CR) at the NASA Goddard Space Flight Center facility in Greenbelt, MD. These tests were conducted with the complete system to validate the end-to-end model of interference fringes. The configuration of the GeoSTAR in the CR is shown in Fig. 5. The test fixture centered the antenna array directly over the azimuth drive at the base of the fixture and directly in line with a polarization drive located behind the array. As shown, the antenna is rotated 90° in polarization relative to that in Figs. 1 and 2. The signal source for the tests consisted of an amplified noise diode which was switched on and off under the control of the GeoSTAR data system. This was placed at the focal point of a large paraboloid reflector (not shown) of the CR which collimates a wavefront—creating in effect an infinitely long antenna range. Data processing involved computing a noise diode deflection from the "ON" and "OFF" states of the source at each test position. Measurements were made every 2° of azimuth and every 5° of polarization. The deflections were calculated for all

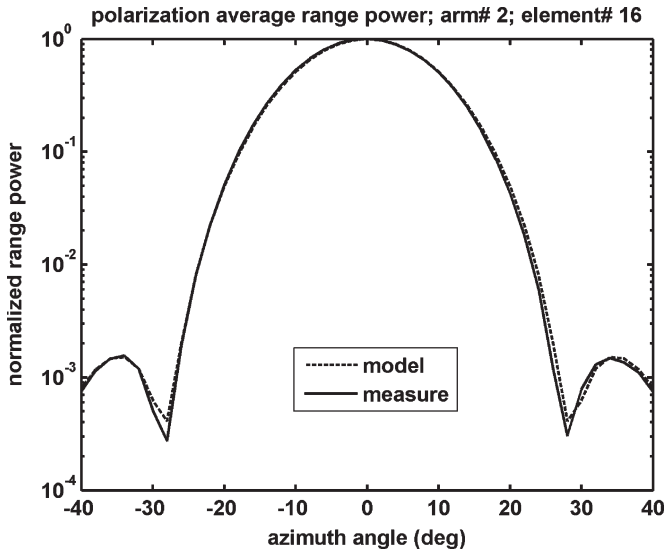

Fig. 6. GeoSTAR antenna patterns as modeled (dashed) and measured (solid) for one of 24 antennas. This pattern was measured with the GeoSTAR correlators using a noise source on the antenna range. An average of 36 different azimuth sweeps at difference polarizations is presented here.

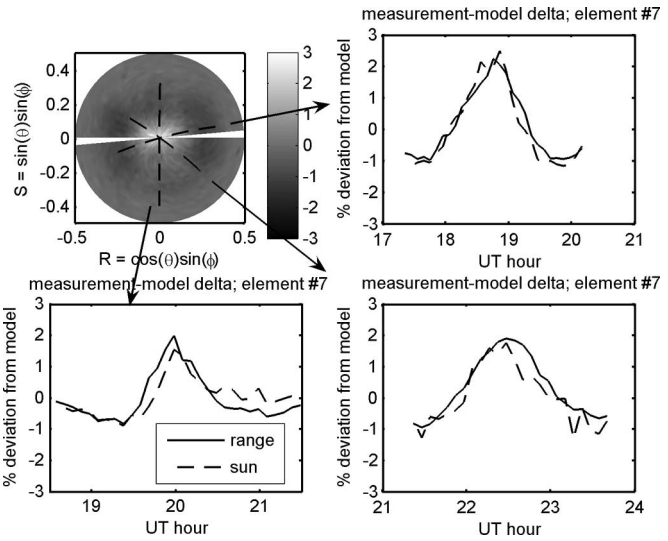

Fig. 7. GeoSTAR antenna pattern error example. Errors are expressed as a percentage relative to the model. The upper left graph is the complete antenna range result, coded such that white represents 3% higher antenna gain than model prediction. The three dashed traces represent the solar transit paths, as observed in three experiments, corresponding to the three graphs below and right. The dashed curves in the graphs are solar measurements, and the solid traces are coincident antenna range measurements.

192 complex correlators of the GeoSTAR array. The amplitude response of each of the 24 elements was then isolated by applying the closure constraint

$$V_{\mathrm{AA}} = \frac{V_{\mathrm{AB}} V_{\mathrm{CA}}}{V_{\mathrm{BC}}} \tag{2}$$

where the subscripts denote the responses formed between any three elements, A, B, and C, of the array. For any single element, there were 64 such combinations in our array; therefore, an average was used. This equation is only valid for the response to a 100% correlated point source; passband and polarization mismatches among elements will also degrade this relation. Data indicate that (2) is reliable to the 0.1% level, based on the consistency among the 64 solutions available for each antenna.

Fig. 6 presents an example antenna response from a preliminary analysis of the antenna range data. An average has been formed from 36 different azimuth scans versus polarization. An overlay of the model is also provided which agrees quite well with the measurements. To date, our model is based entirely on the geometry of the Y-array and on a spherical wave expansion of the elemental horn.

The logarithmic scale in Fig. 6 is insufficient to view the errors below a few percent. A more detailed look at our data reveals typical errors on the order of 2% to 4% relative to the model antenna pattern. When we first examined these errors, we suspected anomalies associated with the CR. The CR design specified only 1 dB of amplitude uniformity within the collimated wavefront, and we indeed observed such anomalies—particularly as the antenna was rotated in polarization. These anomalies were about 100 times larger than our measurement goal. We were able to recover from these effects by the fact that the array was centered on the azimuth and polarization axes of the range. This minimized the array displacements during each azimuth scan and, thereby, mitigated the large amplitude and phase errors of the CR wavefront. To compensate for large variations versus polarization, as well as a drift in source power over the many hours required for these tests, each azimuth scan was normalized to a constant power at the center position. The beam center position was also adjusted slightly in azimuth to correct apparent phase anomalies of the CR. These adjustments brought the measurements to a state that appeared to agree with the models at the 2% level, but these results were still suspect since the CR anomalies were poorly understood. We therefore needed an independent confirmation of the measurement precision. This was achieved by observing the sun in outdoor tests which were conducted several months later.

Solar transit observations were conducted at the JPL by simply pointing the GeoSTAR at the sky and allowing the sun to pass across the FOV for several hours. These data were then processed by subtracting an atmospheric background which was recorded at the end of the test and, then, by using the known elevations from ephemeris data to fit the response to the atmospheric opacity versus elevation above the horizon. These responses were further normalized to a model of the sun visibility versus baseline using a Bessel Function. This correction was small since the sun diameter of 0.6° was small relative to our largest baseline—which resolves 1°.

Fig. 7 summarizes the solar and antenna range responses—each as compared to the model. The scale here is the percentage error relative to the model. The gray-scale image represents the complete measurement of the antenna range, and the three dashed traces in this image indicate the path of the sun through the FOV as observed on three different days. The solar responses are then plotted together with the extracted antenna responses in the three remaining graphs in Fig. 7. The agreement between the solar and antenna range responses here is very good and is typical of the 24 elements

of our array. Overall, the rms difference between the antenna range measurements and the solar responses is typically 0.3%, with a few outliers with errors around 0.6%. This agreement is really quite good, and it indicates that the antenna range data are very reliable. The overall rms errors of either of the measurements (sun or the range), with respect to the model, are in the 0.8%–1.5% range when calculated along the solar transit lines. Peak antenna gains are found to be higher on average than the model would predict, but are in agreement with one another at the 1% level, with outliers at 2% relative to the mean. This result confirms that our system will meet the requirements in the majority of the array in Table I by modeling alone, and that it will be possible to measure the antenna patterns with sufficient accuracy for the few elements near the center of the array.

VII. Conclusion

We have developed a comprehensive error budget for a future geostationary microwave imager and have demonstrated a practical system and a calibration approach that will meet a goal for 1-K accuracy in a large imager with 50-km resolution on the Earth. Our design paid close attention to controlling the antenna patterns and interference fringes. We found that it is possible to build a system which meets the requirements by design, without an extensive campaign to precisely measure a G-matrix for the majority of the array. Only the short baselines of the array need the more precise calibration, and we demonstrated that these measurements are straightforward. These results indicate that the inversion of the image will also be straightforward, since they show that majority of the synthesis processing can be handled by a conventional FFT.

Our design also needed to address some very challenging issues related to biases, quadrature balance, noise performance, and stability. We designed several circuits into our demonstrator so that we could evaluate the merits of various approaches. These included the phase-modulated noise injection circuitry, the amplitude-modulated LNAs, and the phase-switched LO. In the end, the phase-switched LO won out, since it simultaneously solved the null-offset and quadrature balance problems. A single-phase noise diode is the only other calibration device that appears to be necessary to stabilize the system—and only in the short baselines of the array. For the majority of the array, where gain requirements are relaxed, the intrinsic phase and receiver noise are stable enough to meet the requirements without this circuit. This works to our advantage in terms of both cost and noise performance. The noise figure of the GeoSTAR, like any radiometer, is paramount. By eliminating the ferrite isolators and directional coupler in the larger baselines of the array, we expect to gain perhaps 1 dB of improved noise figure.

We conclude with some very preliminary images measured with the GeoSTAR. Figs. 8 and 9 present the images along with reference photographs. These were measured in an uncontrolled ambient environment shortly after the antenna range tests and were synthesized from a simple Fourier series, as discussed in Appendix I, without any corrections for the elemental antenna pattern and without an accurate overall noise temperature calibration. The temperature scales are therefore not reliable. We present them here to merely show that the system is functioning and producing images with good sensitivity and accurate geometry. The images of a hillside in Fig. 8 include a dish antenna which reflects the microwave signal toward the cold sky, and the shape of this dish and of the horizon accurately matches the photograph. Fig. 9 shows an image measured in the near field of a subject holding a cup of hot coffee. Here, we see again the correct shapes, and we see good sensitivity at the ~2-K level.

(a)

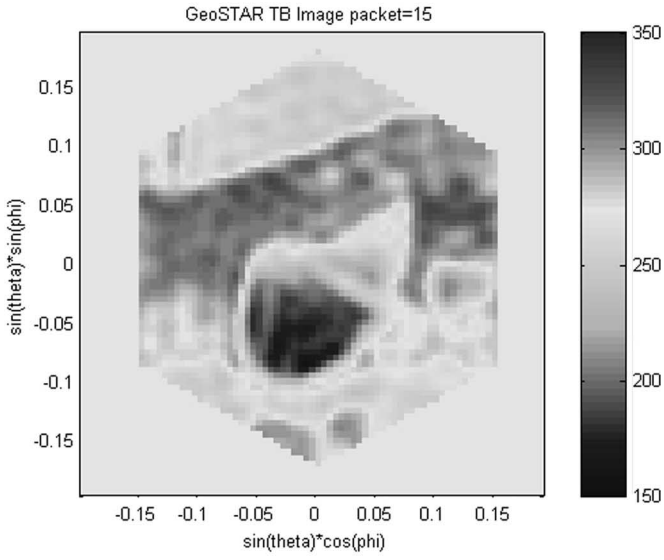

(b)

Fig. 8. (a) GeoSTAR image of hillside at 50.3 GHz with reference photograph. (b) The hexagonal image represents the alias-free region of GeoSTAR.

To provide a quantitative validation of the above error budget, we are presently conducting tests with a large temperature controlled disk target deployed above the GeoSTAR to simulate the Earth disk as viewed from GEO with a cold background. We will examine these results in the coming months. We also plan to use these data to demonstrate various recalibration options for our system. These include the use of the sun as a phase reference as it passed into the aliased regions of the image and the use of the limb itself as a reference. The utility of a ground

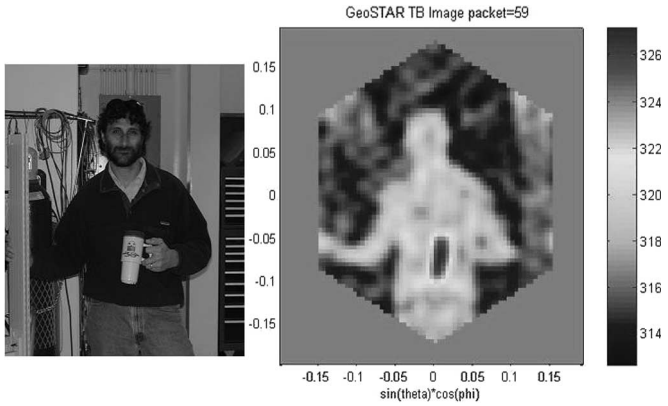

Fig. 9. Near field image of subject with hot coffee in hand.

beacon is also being considered and will be tested as a means to provide a continuous phase reference for the system.

APPENDIX I

Ideally, the visibility function is the Fourier transform of the brightness temperature image as weighted by the elemental antenna pattern in the equation

$$V(u,v) = \iint\limits_{r^2+s^2\le 1} T(r,s)\frac{|f(r,s)|^2}{\Omega\sqrt{1-r^2-s^2}} \times \exp\left[-j2\pi(ru+sv)\right] drds \quad \text{(A1)}$$

where r and s are the horizontal and vertical coordinates of the image plane (also referred to as the directional cosines) defined in terms of spherical coordinates by

$$r \equiv \sin\theta\cos\varphi$$
$$s \equiv \sin\theta\sin\varphi. \quad \text{(A2)}$$

$T(r,s)$ is the brightness temperature image, $f(r,s)$ represents the normalized antenna voltage pattern, Ω is the beam solid angle of the antenna, and u and v are the respective horizontal and vertical spacings between elements of the array—given here as wavenumbers. For the moment, (A1) neglects other terms detailed by Camps *et al.* [5] and by Corbella *et al.* [10], which are necessary to model antenna mismatches, mutual coupling, passband mismatches, fringe wash, array alignment, etc. These are discussed below.

By identity of (A1) with the Fourier series, the image synthesis takes one of two forms. The first applies to the GEO Earth observation where the Earth is contained within the UaFOV and surrounded by approximately 0 K. In this case, the integral of (A1) is limited precisely to one interval of the hexagonally periodic Fourier series such that

$$T(r,s) \cong \frac{\Omega\sqrt{1-r^2-s^2}}{A_{\rm u}\,|f(r,s)|^2} \times\Big\{V(0,0)+2\sum_i \mathrm{Re}\left[V(u_i,v_i)\right]\cos[2\pi(ru_i+sv_i)] + \mathrm{Im}\left[V(u_i,v_i)\right]\sin\left[2\pi(ru_i+sv_i)\right]\Big\} \quad \text{(A3)}$$

where i is an index for the u-v sample in Fig. 2 and $A_{\rm u}$ is the area of one hexagonal period [7] in the r-s plane given by

$$A_{\rm u} = \frac{2\lambda^2}{d^2\sqrt{3}} \quad \text{(A4)}$$

which equals to 0.081 in the present design at 50.3 GHz and 2.25-cm element spacing. Our antenna has a beam solid angle of 0.135; therefore, we see that the fraction on the left side of (A3) is 1.66 near boresight. This is a factor which amplifies errors in our system (i.e., noise and biases).

The other synthesis case applies to ground-based observations where the brightness temperature surrounding the main synthesis region is unknown. In this case, the aliased regions are superimposed (added) to the main region. In these instances, the "best" synthesis approach appears to be the simplest case of

$$T(r,s) \cong V(0,0) + 2\sum_i \mathrm{Re}\left[V(u_i,v_i)\right]\cos\left[2\pi(ru_i+sv_i)\right] + \mathrm{Im}\left[V(u_i,v_i)\right]\sin\left[2\pi(ru_i+sv_i)\right]. \quad \text{(A5)}$$

APPENDIX II

The G-matrix approach lumps all the gain errors into a single empirical function g which (in complex form) replaces (A1) with

$$V(u,v) = \iint\limits_{r^2+s^2\le 1} T(r,s)g(r,s,u,v)drds. \quad \text{(A6)}$$

The matrix form of this is

$$V = GT \quad \text{(A7)}$$

where V is a vector of M visibility samples and T is a vector of P image pixels, with $P > M$. This is the original formulation of reference [3]. In essence, G is treated as an arbitrary function to be determined entirely by measurement and then inverted by the orthogonal projection theorem according to

$$G' = G^{\rm t}(GG^{\rm t})^{-1}. \quad \text{(A8)}$$

One problem with this formulation is that the matrix inversion of (A5) is very large and very sensitive to small sampling errors. This has already become apparent even in our small demonstrator instrument, with $M = 385$. We anticipate that this inversion may be impractical in this form and probably unnecessary in a large spaceborne system ($M = 60\,000$). More recently, we have reformulated the problem with what we call the "flat" G-matrix by casting (A1) in the form

$$V(u,v) = \iint\limits_{r^2+s^2\le 1} T(r,s)\frac{|f(r,s)|^2}{\Omega\sqrt{1-r^2-s^2}}g(r,s,u,v)drds \quad \text{(A9)}$$

which takes the matrix form

$$V = \mathrm{GFT} \quad \text{(A10)}$$

where F is a $P \times P$ diagonal matrix which represents the ideal elemental antenna pattern and G is composed of discrete samples of the complex exponent in (A1). This new formulation has the advantage that the product GG^{t} in (A8) is diagonal in the ideal case. This reduces the inversion of (A8) to a transpose operation if the array is well behaved. If not—if the elemental patterns are not well behaved—we propose to lump all complex gain errors (antenna errors, fringe wash, etc.) into G while maintaining a common ideal model of the antenna pattern F. This form is readily adapted to a hybrid synthesis in which large baselines of the array (which are sufficiently well behaved) may be processed with a conventional FFT. The short baselines (where sensitivity to error is high) can be processed by the G-matrix. These two solutions can be merged onto a common image plane and, then, normalized with the common ideal antenna pattern [as in (A3)]. This approach reduces the size of the inversion in (A8) to an appropriate level and eases the processing load for the overall system.

ACKNOWLEDGMENT

This work has been carried out at the Jet Propulsion Laboratory, California Institute of Technology under a contract with the National Aeronautics and Space Administration. The first author, A. B. Tanner, would like to thank the coauthors from University of Michigan for a superb data system, S. Seufert and K. Hersey for their outstanding work on the antenna range, and especially W. A. Imbriale at JPL for a most innovative antenna design.

REFERENCES

[1] B. Lambrigtsen, W. Wilson, A. Tanner, T. Gaier, C. Ruf, and J. Piepmeier, "GeoSTAR—A microwave sounder for geostationary satellites," in *Proc. IEEE IGARSS*, 2004, vol. 2, pp. 777–780.

[2] C. S. Ruf, C. T. Swift, A. B. Tanner, and D. M. Le Vine, "Interferometric synthetic aperture microwave radiometry for the remote sensing of the Earth," *IEEE Trans. Geosci. Remote Sens.*, vol. 26, no. 5, pp. 597–611, Sep. 1988.

[3] A. B. Tanner and C. T. Swift, "Calibration of a synthetic aperture radiometer," *IEEE Trans. Geosci. Remote Sens.*, vol. 31, no. 1, pp. 257–267, Jan. 1993.

[4] I. Corbella, F. Torres, A. Camps, A. Colliander, M. Martín-Neira, S. Ribó, K. Rautiainen, N. Duffo, and M. Vall-llossera, "MIRAS end-to-end calibration: Application to SMOS L1 processor," *IEEE Trans. Geosci. Remote Sens.*, vol. 43, no. 5, pp. 1126–1134, May 2005.

[5] A. Camps, I. Corbella, F. Torres, N. Duffo, M. Vall-llosera, and M. Martín-Neira, "The impact of antenna pattern frequency dependence in aperture synthesis microwave radiometers," *IEEE Trans. Geosci. Remote Sens.*, vol. 43, no. 10, pp. 2218–2224, Oct. 2005.

[6] A. Camps, J. Bará, F. Torres, I. Corbella, and J. Romeu, "Impact of antenna errors on the radiometric accuracy of large aperture synthesis radiometers. Study applied to MIRAS," *Radio Sci.*, vol. 32, no. 2, pp. 657–668, Mar./Apr. 1997.

[7] A. Camps, J. Bará, I. Corbella, and F. Torres, "The processing of hexagonally sampled signals with standard rectangular techniques: Application to 2D large aperture synthesis interferometric radiometers," *IEEE Trans. Geosci. Remote Sens.*, vol. 35, no. 1, pp. 183–190, Jan. 1997.

[8] J. Bará, A. Camps, F. Torres, and I. Corbella, "Angular resolution of two-dimensional, hexagonally sampled interferometric radiometers," *Radio Sci.*, vol. 8, no. 5, pp. 1459–1473, Sep./Oct. 1998.

[9] J. B. Hagen and D. T. Farley, "Digital correlation techniques in radio science," *Radio Sci.*, vol. 8, no. 8/9, pp. 775–784, Aug./Sep. 1973.

[10] I. Corbella, N. Duffo, M. Vall-llosera, A. Camps, and F. Torres, "The visibility function in interferometric aperture synthesis radiometry," *IEEE Trans. Geosci. Remote Sens.*, vol. 42, no. 8, pp. 1677–1682, Aug. 2004.

Alan B. Tanner received the B.S. and Ph.D. degrees from University of Massachusetts at Amherst, in 1984 and 1989, respectively.

He is a Microwave Systems Engineer with the Jet Propulsion Laboratory (JPL), California Institute of Technology, Pasadena. His work with JPL has focused on the design and calibration of radiometers and radar scatterometers for remote sensing.

William J. Wilson (S'59–M'64–SM'86–F'98) received the B.S.E.E. degree from University of Washington, Seattle, in 1961, and the M.S.E.E., E.E., and Ph.D. degrees in electrical engineering from Massachusetts Institute of Technology, Cambridge, in 1963, 1964, and 1970, respectively.

He recently retired after a distinguished career with the Jet Propulsion Laboratory (JPL), California Institute of Technology, Pasadena. In 1964, he served in the U.S. Air Force. In 1970, he joined the Aerospace Corporation where he developed millimeter wave receivers and for radio astronomy observations. From 1976 to 1977, he was an Assistant Professor with the Electrical Engineering Department, University of Texas, Austin. In 1980, he joined the JPL where he developed numerous low-noise microwave and millimeter wave radiometers and radar systems for Earth remote sensing. He has published more than 160 technical papers and reports.

Bjorn H. Lambrigsten joined the Jet Propulsion Laboratory (JPL) in 1982. He specializes in atmospheric remote sensing and related research. He is the GeoSTAR Principal Investigator and leads a number of other efforts as well, including hurricane-related research. He is a member of the NPOESS Preparatory Project science team, is the Microwave Instrument Scientist for the Atmospheric Infrared Sounder project, and leads the AIRS Atmospheric Science Group at JPL.

Steve J. Dinardo (M'04–A'04) received the B.S.E.E. degree from California State University, Los Angeles, in 1983.

In 1978, he joined the NASA Jet Propulsion Laboratory (JPL), California Institute of Technology, Pasadena, where he has been involved in mobile VLBI, orbiting VLBI, GPS development, aircraft polarimetric wind radiometers (WINDRAD), JPL's aircraft rain radar, and a 94-Ghz cloud profiling radar. He built the JPL Ku-band polarimetric scatterometer (POLSCAT) deployed on the NCAR C-130. He is currently involved in the development of low-noise microwave radiometers and radar systems for aircraft and spacecraft for remote sensing of soil moisture and ocean salinity and GeoSTAR. He is a Senior Engineer of JPL.

Shannon T. Brown (S'02–M'05) received the B.S. degree in meteorology from Pennsylvania State University, University Park, and the M.S. and Ph.D. degrees from University of Michigan, Ann Arbor, in 2005.

In 2005, he joined the NASA Jet Propulsion Laboratory, California Institute of Technology, Pasadena, as a member of the engineering staff in the Microwave Advanced Systems section. His research interests include microwave radiometer calibration and geophysical algorithm.

Pekka P. Kangaslahti received the M.Sc. and Ph.D. degrees in electrical engineering from Helsinki University of Technology, Espoo, Finland, in 1992 and 1999, respectively.

Since 1999, he has been with the Jet Propulsion Laboratory, California Institute of Technology, Pasadena, first as a Visiting Engineer and currently as a Senior Engineer. His main research interests include monolithic millimeter wave integrated circuits (MMICs) and MMIC module technology.

Todd C. Gaier received the Ph.D. degree in physics from University of California, Santa Barbara, in 1993.

He is the Supervisor of the Microwave Astrophysics and Earth Science Systems Group, Jet Propulsion Laboratory, California Institute of Technology, Pasadena. His research interests include millimeter wave electronics for applications in astrophysics and Earth remote sensing. His group develops technologies and instruments using monolithic microwave integrated circuit (MMIC) components operating at frequencies of 10–250 GHz. Active projects in the group include the Planck-LFI mission to study the anisotropy and polarization of the cosmic microwave background (CMB); the Q/U Imaging Experiment (QUIET) exploring the polarization of the CMB; GeoSTAR, an interferometric synthetic aperture imager for Earth atmospheric sounding from geostationary orbit and the advanced microwave radiometers for the Jason-II Mission mapping small variations in sea level across the globe monitoring conditions such as El-Niño.

Christopher S. Ruf (S'85–M'87–SM'92–F'01) received the B.A. degree in physics from Reed College and the Ph.D. degree in electrical and computer engineering from University of Massachusetts, Amherst.

He is a Professor of atmospheric, oceanic, and space sciences and electrical engineering and computer science, and a Director of the Space Physics Research Laboratory, University of Michigan, Ann Arbor. He has worked previously with Intel Corporation, Hughes Space and Communications, the NASA Jet Propulsion Laboratory, and Penn State University. In 2000, he was a Guest Professor with the Technical University of Denmark. He has published over 97 refereed articles in the areas of microwave remote sensing instrumentation and geophysical retrieval algorithms.

Dr. Ruf is a member of the AGU, AMS, and URSI Commission F. He has received three NASA Certificates of Recognition and four NASA Group Achievement Awards, as well as the 1997 GRS-S Transactions Prize Paper Award and the 1999 IEEE Judith A. Resnik Technical Field Award. He has served or is serving on the editorial boards of the *IEEE GRS-S Newsletter*, *AGU Radio Science*, IEEE TRANSACTIONS ON GEOSCIENCE AND REMOTE SENSING and the *AMS Journal of Atmospheric and Oceanic Technology*.

Steven M. Gross received the B.S. and M.S. degrees in electrical engineering, and the M.B.A. degree, all from Michigan State University, East Lansing, in 1990, 1993, and 2000, respectively.

He is a member of the engineering staff of the Space Physics Research Laboratory (SPRL), University of Michigan, Ann Arbor. Prior to joining SPRL, he was a member of the technical staff with the High Energy Physics group, Michigan State University, and with the TRW corporation. His primary engineering activities involve high-speed digital logic and field-programmable gate array design.

Mr. Gross was the recipient of the 2004 NASA Group Achievement Award as a member of the Lightweight Rainfall Radiometer Instrument Team.

Boon H. Lim received the B.S. and M.S. degrees in electrical engineering from University of Michigan, Ann Arbor, in 1999 and 2001, respectively. He is currently working toward the Ph.D. degree with the Remote Sensing Group at the University of Michigan.

His research interests include synthetic aperture array radiometer design and calibration.

Stephen B. Musko received the B.S. degree in computer science from Eastern Michigan University, Ypsilanti, in 1985.

He is a member of the engineering staff of the Space Physics Research Laboratory, University of Michigan, Ann Arbor. His primary engineering activities involve high-speed data and embedded real-time software systems design.

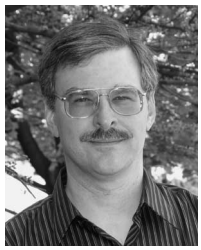

Steven A. Rogacki received the B.S. degree in electrical engineering from the University of Michigan, Ann Arbor, in 1987.

He worked to develop industrial sensors, automation, and medical instrumentation before joining the engineering staff at the Space Physics Research Laboratory (SPRL), University of Michigan in 1997. At SPRL, he has designed instrumentation for a number of space related and terrestrial research projects. His work includes analog and digital circuit designs, high-speed analog-to-digital conversion, and time-to-digital conversion using FPGA devices.

Mr. Rogacki is a Licensed Engineer in the state of Michigan.

Jeff R. Piepmeier received the B.S. degree from LeTourneau University, Longview, TX, in 1993, and the M.S. and Ph.D. degrees from Georgia Institute of Technology, Atlanta, in 1994 and 1999, respectively.

He is with the NASA's Goddard Space Flight Center (GSFC), Greenbelt, MD. His work with the GSFC has focused on microwave radiometer technology development for Earth remote sensing.